actuators

MDPI

Article

Preload-Dependent Protective Reaction Latency in a Pneumatic Artificial Muscle-Actuated Humanoid Joint

Dávid Kóczi * and József Sárosi

Department of Mechatronics and Automation, Faculty of Engineering, University of Szeged, 6720 Szeged, Hungary; sarosi@mk.u-szeged.hu
* Correspondence: koczid@mk.u-szeged.hu

Abstract

Humanoid robots operating near humans require short protective reaction times in physical human–robot interaction (pHRI). Safety standards distinguish between quasi-static and transient contact. This paper quantifies the reaction timing of a compliant pneumatic artificial muscle (PAM) mechanism under controlled preload conditions. Measurements were performed at 10 N, 50 N, and 100 N preload using synchronised load-cell force, PAM pressure, actuator position, and force-sensitive resistor (FSR) signals. Reaction timing was evaluated relative to the FSR-defined contact onset, at which the controller issued the pressure-release command. The force trace reached its first post-contact peak within 15–20 ms after onset, while the pressure peak occurred within 5–15 ms. A 90% recovery of the post-contact force excursion was achieved within 40–50 ms, whereas the corresponding pressure excursion required 155–180 ms. These timing results quantify reaction latency in PAM-actuated humanoid joints and support multi-modal sensing for robust onset localisation and mitigation monitoring in both ISO/TS 15066 contact types.

Keywords: humanoid robot safety; physical human–robot interaction; pneumatic artificial muscle; preload; collision reaction

1. Introduction

This work measures the collision reaction latency of a pneumatic artificial muscle (PAM) driven mechanism during quasi-static and transient contact, and it investigates the effect of preload. ISO/TS 15066 treats these contact types separately because quasi-static contact can clamp tissue, while transient contact is a short impact with recoil and different biomechanical limits [1]. The results are therefore reported for both types.

Reaction latency is an end-to-end time measure that includes detection, decision logic, and actuation. Any delay increases the impulse delivered before the robot reacts [2]. This is particularly critical in fast impacts, where peak forces may occur before the control system can react [3]. For humanoid robots, reaction latency must be verified on the target hardware, as effective inertia and contact dynamics depend on configuration [4].

Prior work in physical human–robot interaction (pHRI) reviews contact events, collision detection, and mitigation strategies [4]. For transient impacts, impulse and energy are useful in addition to peak force [5]. PAM dynamics are nonlinear, and models show that bandwidth depends on pressure and operating point [6–8]. However, experimental timing data under controlled preload remain limited. The aim of this paper is to quantify, in measurable terms, how quickly the mechanism begins to react after contact detection for both ISO/TS 15066 contact types [1].

Check for updates

Academic Editors: Yanhong Peng, Fangchao Hu and Yi Li

Received: 24 April 2026
Revised: 18 May 2026
Accepted: 18 May 2026
Published: 19 May 2026

Copyright: © 2026 by the authors. Licensee MDPI, Basel, Switzerland. This article is an open access article distributed under the terms and conditions of the Creative Commons Attribution (CC BY) license.

The main contributions of this study are as follows. First, the study defines a contact-onset and reaction-time evaluation procedure based on synchronised force, pressure, position, and FSR signals. Second, it reports reaction-latency metrics for quasi-static and transient contact at 10 N, 50 N, and 100 N preload. Third, it evaluates severity-related engineering proxies, including the time to force peak, the impulse until the force peak, and an early-time stiffness estimate. Finally, the study provides design-oriented guidance for allocating sensing and actuation latency in PAM-actuated humanoid safety layers.

Collision detection and safe reaction have been studied extensively for torque-controlled and compliant robots. Many methods use internal signals and do not require external sensors [9,10]. Energy-based measures are also used for contact detection [10]. In practice, detection sensitivity must be balanced against false positives caused by noise and model uncertainty. After detection, common reactions include stopping, retreating, and impedance-based force limitation [11,12].

ISO/TS 15066 defines quasi-static and transient contact and provides separate biomechanical limits for collaborative safety assessment [1]. In fast impacts, impulse and energy transfer can be more informative than peak force alone [13]. In practice, these limits are applied together with the broader requirements of ISO 10218 during risk assessment [14].

PAM actuation is common in soft and lightweight mechanisms. It provides a high force-to-weight ratio and intrinsic compliance [15]. The pressure-force-length relation is nonlinear, and the dynamics include hysteresis and friction, which limit response bandwidth [6,8]. Preload changes the operating point, so it can change effective stiffness and the pressure response during contact.

Service and humanoid robots plan to operate close to people and must tolerate incidental contacts. In these settings, safety cannot rely only on separation. Typical solutions combine mechanical compliance, force/impedance control, and external sensing [16]. ISO 13482 provides additional guidance for personal-care robots [17].

FSR sensors are attractive as low-cost onset triggers, but resistive sensing exhibits nonlinearity, drift, and hysteresis, which limit quantitative force estimation [18]. Complementary safety layers can employ whole-body tactile and proximity skins for contact localisation and pre-contact mitigation [19–22], while broader touch-technology surveys highlight integration trade-offs across tactile modalities [23]. Model-based collision detection and reaction using proprioception provides an alternative or redundant channel for onset estimation [24]. For PAM-driven joints, pneumatic valve dynamics can be a non-negligible contributor to the overall reaction-time chain [25], and PAM architecture and application surveys provide context for operating-point-dependent actuation dynamics [26,27]. Passive coverings can further reduce impact severity [28], and posture-dependent reflected-mass metrics support configuration-aware risk assessment in pHRI [29]. Recent multi-modal tactile-proximity systems illustrate practical fusion approaches that complement latency-focused characterisation [30].

The intention of this study is to provide hardware-level timing evidence for a simplified PAM-actuated joint surrogate. The study does not aim to certify a complete humanoid robot or to define general biomechanical injury thresholds. Instead, it provides a reproducible experimental procedure and baseline latency data for future safety validation of PAM-actuated mechanisms.

Section 2 describes the experimental setup, the collision scenarios, and the signal processing used to extract timing metrics. Section 3 reports the measured reaction latency results for quasi-static and transient contact at 10 N, 50 N, and 100 N preload. Section 4 discusses the implications of safety-layer reaction-time requirements for PAM-actuated humanoid joints and highlights their limitations. Section 5 concludes the paper.

2. Materials and Methods

Experiments were conducted on a simplified test platform representing a compliant humanoid joint segment actuated by a pneumatic artificial muscle (PAM). The rig was previously used to analyse collision types [31]. Here, it is used to quantify reaction timing under controlled preload conditions. As shown in Figure 1, the setup enables controlled preload application and repeatable quasi-static and transient contact conditions. Synchronised signals were recorded from a load cell, a pressure sensor, a position sensor, and a force-sensitive resistor (FSR) mounted at the contact interface.

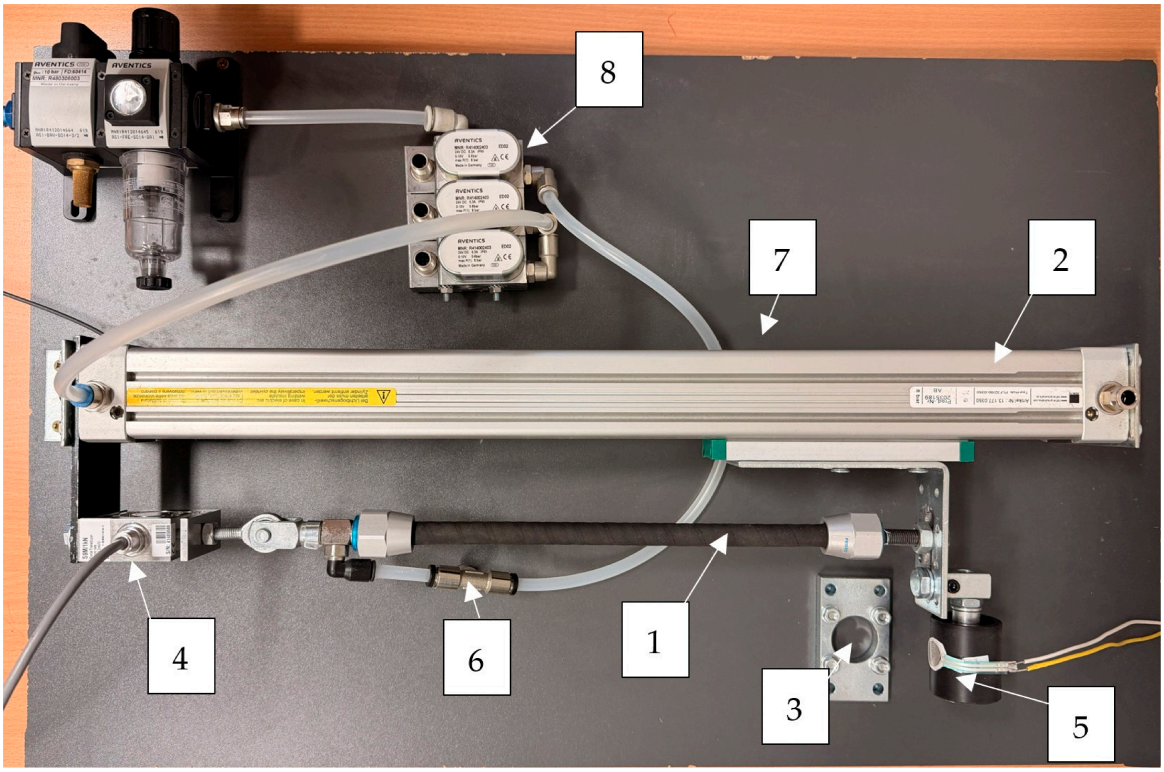


Figure 1. Measurement system overview. (1) PAM actuator, (2) rodless cylinder, (3) collision interface, (4) load cell, (5) FSR, (6) pressure sensor, (7) position sensor, (8) proportional valves.

2.1. Measurement System

The actuator was a Festo MAS-10-40N-AA pneumatic artificial muscle (Festo SE & Co. KG, Esslingen am Neckar, Germany). In the notation used for the PAM model, L denotes the active muscle length, and d denotes the internal muscle diameter. For the investigated MAS configuration, these parameters were L = 250 mm and d = 10 mm. The actuator is capable of approximately 25% contraction at 0.8 MPa. The PAM is mounted on a 32 mm diameter Hafner PLF32 rodless cylinder (Hafner-Pneumatik Krämer KG, Kornwestheim, Germany), which provides back-pressure force to emulate static loads and to set repeatable preload conditions. Both components are controlled via independent AVENTICS™ ED02 proportional valves (Emerson Automation Solutions/AVENTICS GmbH, Laatzen, Germany) [31].

As shown in Figure 2, four synchronised sensing modalities were used:

1. Load cell: a precision S9M/1 kN force transducer (HBK—Hottinger Brüel & Kjær, Darmstadt, Germany) mounted via a ball joint to measure axial force in the actuation line.

2. Position sensor: a Rexroth SM6-AL analogue displacement sensor (Bosch Rexroth AG, Lohr am Main, Germany) mounted on the cylinder to infer PAM contraction through piston position.
3. Pressure sensor: a Festo SPTE-571484 (Festo SE & Co. KG, Esslingen am Neckar, Germany) analogue pressure transducer measuring PAM internal pressure.
4. FSR (Force-Sensitive Resistor): a Legact FSR RP-C18,3-LT (Shenzhen Legact Technology Co., Ltd., Shenzhen, China) force-sensitive resistor mounted between the colliding surfaces at the collision interface for direct contact onset detection.

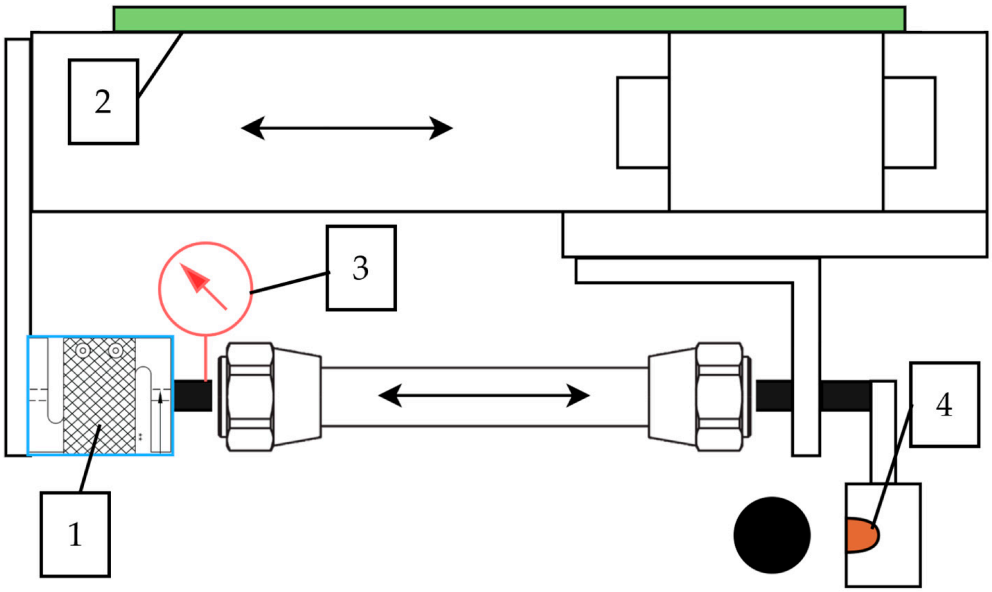


Figure 2. Sensor positions in the PAM-actuated collision test bench: (1) S9M/1 kN load cell, (2) Rexroth SM6-AL analogue position sensor, (3) Festo SPTE pressure sensor, and (4) Legact FSR contact sensor mounted at the collision interface.

The control core was an NI myRIO-1900 (National Instruments Corporation, Austin, TX, USA) controller. It processed the analogue sensor signals, commanded the proportional valves, and streamed the data to a host PC. The control software was developed in LabVIEW (NI Labview 2019). In the measurement mode, an adjustable threshold on the FSR signal was used to trigger the recording of a fixed-length dataset around the impact [31]. At the same threshold, which marks contact onset at the interface, the controller issued the pressure release command, and the acquisition included a pre-onset interval. Due to the myRIO platform constraints, the sampling interval was fixed at T_s = 5 ms because faster sampling was not feasible in the used configuration.

Consequently, the extracted timing metrics are quantised in 5 ms increments. Events occurring between two samples, including valve-response onset and very early force peaks, cannot be resolved separately. Therefore, the reported latency values should be interpreted as sampled end-to-end timing estimates rather than as sub-millisecond actuator or valve response measurements.

The exported data represent controller-processed synchronised samples. For each preload and contact condition, the myRIO controller stored the pointwise-averaged trace from ten repeated trials. No additional offline averaging was applied after export. The present analysis uses these controller-stored averaged synchronised time series.

The overall pneumatic system has a simple architecture, as illustrated in Figure 3. It starts with an air preparation unit that supplies the system at a constant pressure of 0.6 MPa.

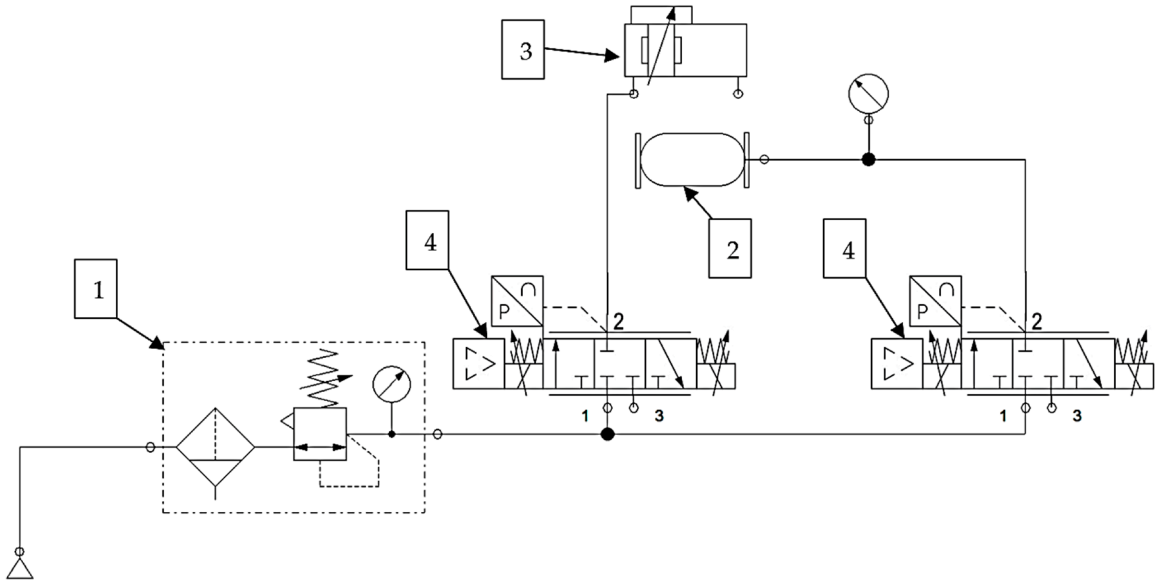


Figure 3. Pneumatic control diagram: (1) air preparation unit, (2) Festo MAS-10-40N-AA pneumatic artificial muscle, (3) Hafner PLF32 rodless cylinder, and (4) AVENTICS Series ED02 proportional valves.

As shown in Figure 4, the test rig is instrumented and controlled via a National Instrument myRIO unit. The position and pressure sensors, the load cell, and the force-sensitive resistor provide the measurement inputs. The myRIO simultaneously commands two proportional valves to regulate the pneumatic actuation and streams the synchronised data to a host PC for logging and analysis.

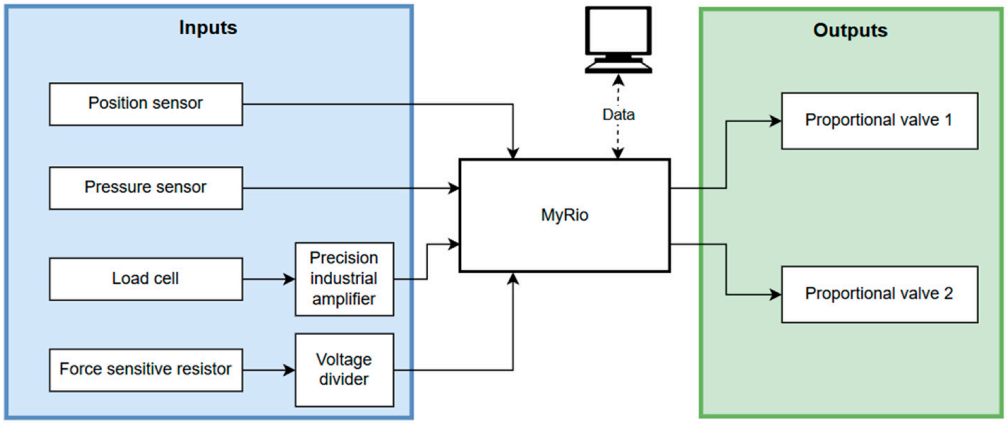


Figure 4. Control and data-acquisition architecture.

2.2. Collision Scenarios and Test Protocol

Two contact types were implemented by changing the boundary condition at the collision object:

- Quasi-static contact: the collision object was fixed, producing a clamp-like boundary condition.
- Transient contact: the collision object could move, producing a short dynamic impact with recoil/separation and a faster decay.

Preload levels were set to 10 N, 50 N, and 100 N. Each scenario was recorded with a sampling interval of 5 ms. Each condition was repeated ten times. The myRIO controller was configured to store the pointwise-averaged signals from the ten repeated trials. There-

fore, the retained dataset contains one averaged synchronised trace for each preload and contact condition.

Because the individual trial records were not retained, standard deviation, confidence intervals, repeatability bands, and outlier analysis cannot be reconstructed from the available dataset. The reported values, therefore, represent metrics extracted from the controller-stored pointwise average of ten trials per condition. This limitation reduces the statistical generalisability of the results, but it does not affect the stated aim of reporting representative hardware-level latency trends for the tested configuration.

The time-aligned traces include only a short pre-onset interval before collision. During this interval, the PAM was already under active tension. Consequently, the pre-onset baseline force F_{base} represents the instantaneous actuator tension at the operating point and may differ from the nominal preload setpoint.

Figure 5 shows an example of the synchronised measurement signals for quasi-static contact at the 10 N preload setpoint. Each record contains 105 samples, including a pre-onset baseline interval and the post-onset response. The dataset, therefore, captures both the pre-onset baseline and the early response dynamics. The onset point was defined as the first sampled instant when the FSR voltage exceeded the threshold value of 0.1 V. At this instant, the controller issued the pressure-release command. The 0.5 s observation interval is relevant because ISO/TS 15066 specifies that, for transient contact, the force/pressure must fall back below the quasi-static limit within 0.5 s [1]. To clarify the standard's acceptance logic, Figure 6 provides a conceptual illustration of how the quasi-static and transient force/pressure limits are interpreted over time according to ISO/TS 15066 [1].

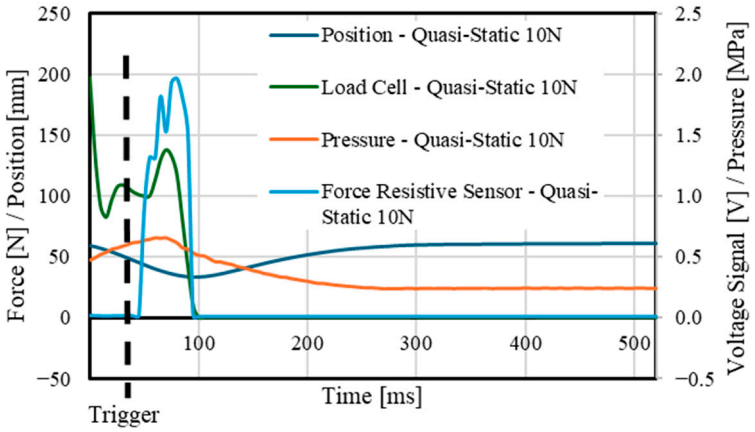


Figure 5. Example synchronised measurement signals—Quasi-static contact, 10 N preload setpoint.

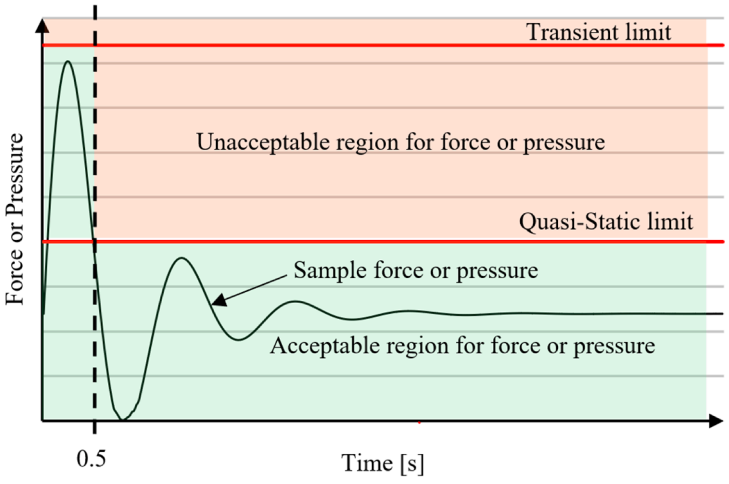


Figure 6. Graphical representation of acceptable and unacceptable forces or pressures.

2.3. Signal Processing

The mathematical relationship between internal pressure, contraction, and the resulting PAM force dictates the structural stiffness prior to collision. According to the virtual work principle, the theoretical pulling force depends on the internal pressure (P), the nominal cross-sectional area (A), and a non-linear function of the contraction ratio (ε) [32]. This can be expressed as:

$$F_{\mathrm{PAM}} = P \cdot A \cdot \left[a(1-\varepsilon)^2 - b\right] \tag{1}$$

where 'a' and 'b' are geometric constants. As preload increases, the internal pressure P must be elevated by the controller to maintain equilibrium. This shifts the operating point and can change the effective stiffness of the actuator and the force–pressure response during contact.

Pearson's correlation coefficient r was used as a descriptive measure of the linear association between the temporally aligned FSR voltage and load-cell force samples within the evaluated time window. The coefficient ranges from -1 to +1, where +1 indicates a perfect positive linear relationship, 0 indicates no linear relationship, and -1 indicates a perfect negative linear relationship. In this study, r is interpreted only as an indicator of sensor-signal similarity, not as proof of calibrated force measurement, because the FSR response is nonlinear and the time-series samples are not independent experimental observations. No statistical significance test was attached to r because the normality and independence assumptions required for inferential use were not evaluated.

$$r = \frac{n\sum(xy) - (\sum x)(\sum y)}{\sqrt{\left[n\sum x^2 - (\sum x)^2\right]\left[n\sum y^2 - (\sum y)^2\right]}} \tag{2}$$

Contact onset time t_0 was defined using the FSR threshold event. Specifically, t_0 was the first sampled time instant t_k where the FSR voltage $V_{FSR}(tk)$ exceeded the fixed threshold V_{th} = 0.1 V. At t_0, the controller issued the pressure-release command. The recorded trace includes pre-onset samples. All other signals were aligned to t_0 before metric extraction. Because the FSR is placed between the colliding surfaces at the contact interface, the threshold crossing was treated as contact onset.

The 0.1 V FSR threshold was selected as a practical contact-onset trigger because it was above the pre-contact baseline level in the retained signals and provided a consistent trigger point for the evaluated scenarios. The FSR was not used as an absolute force sensor. No systematic threshold-sensitivity study was performed; therefore, small changes in Vth may shift t0 by one or more 5 ms samples, especially near low-amplitude or short-duration contacts.

$$t_0 = \min\{t_k \mid V_{\mathrm{FSR}}(t_k) \geq V_{\mathrm{th}}\} \tag{3}$$

After alignment, the following timing metrics were computed for each scenario using the post-contact samples:

- Time to pressure peak, ΔtP,peak: time from t0 to the first maximum of the PAM pressure trace after onset.
- Time to force peak, ΔtF,peak: time from t0 to the first maximum of the load-cell force trace after onset. In this work, ΔtF,peak is used as a proxy for the onset of force reduction, because the force trace transitions from increasing to decreasing at the peak.
- Time to 90% drop, Δts,90: time from t0 until the signal s(t) has decayed by 90% of the peak to minimum excursion observed after the peak (s = force or pressure).
- The 90% drop time was computed with respect to the post-peak minimum smin observed in the recorded window. The time Δts,90 is the earliest time after the peak when s(t) $\leq$ s90.

$$s_{90} = s_{min} + 0.1\left(s_{peak} - s_{min}\right) \tag{4}$$

To relate timing to potential injury-relevant quantities, two additional severity proxies were computed:

Impulse until the force peak,

$$J_{peak} = \int_{t_0}^{t_{F,peak}} F(t)dt \tag{5}$$

approximated by trapezoidal integration on the sampled points.

Early-time stiffness proxy,

$$\hat{k} = \left| \frac{F_{peak} - F(t_0)}{x\left(t_{F,peak}\right) - x(t_0)} \right| \tag{6}$$

using actuator position x(t) from t_0 to the force peak.

In addition, two mitigation-oriented metrics were extracted from the aligned force and FSR signals. The baseline force level F_{base} was defined as the mean load-cell force in the 25 ms interval preceding onset from $t_0 - 25$ ms to t_0. Time to return below baseline, $\Delta t_{F,base}$, was defined as the earliest time after the post-contact force peak at which $F(t) \leq F_{base}$ requiring two consecutive samples to suppress threshold chatter.

Contact release time was derived from the FSR signal. The release instant t_{off} was defined as the earliest sampled time after onset at which $V_{FSR}(t) < Vth$ for at least three consecutive samples. The corresponding contact duration metric is $\Delta t_{off} = t_{off} - t_0$.

Because the sampling interval is 5 ms, timing results are quantised to multiples of 5 ms.

3. Results

3.1. Time-Aligned Response Curve

All signals were aligned to the FSR-defined contact onset t_0 as described in Section 2.3. Figures 7 and 8 show the load-cell force responses for quasi-static and transient contact, respectively, for the three preload setpoints. The curves illustrate a rapid increase to a post-contact force maximum followed by a fast decay. The force peak time provides an upper-bound estimate on how quickly the system begins to reduce the contact force after detecting contact. Figures 8 and 9 show the corresponding PAM pressure responses, highlighting a similar early peak followed by a much slower decay due to pneumatic flow limitations.

Figure 7 presents the aligned load-cell force responses for quasi-static contact at 10 N, 50 N, and 100 N preload setpoints.

Figure 8 presents the aligned load-cell force responses for transient contact at 10 N, 50 N, and 100 N preload setpoints. Following the impact, the measured force does not return to the initial preload level but stabilises at a shifted quasi-static equilibrium. This indicates that the collision alters the contraction state of the PAM and redistributes the internal pressure, resulting in a new operating point. The mechanical force decays faster than the pneumatic pressure equalises, which explains the residual force offset. The effect becomes more pronounced at higher preload levels due to the increased effective stiffness of the system.

Figure 9 compares the corresponding PAM pressure responses for quasi-static contact.

Figure 10 shows the PAM pressure responses for transient contact.

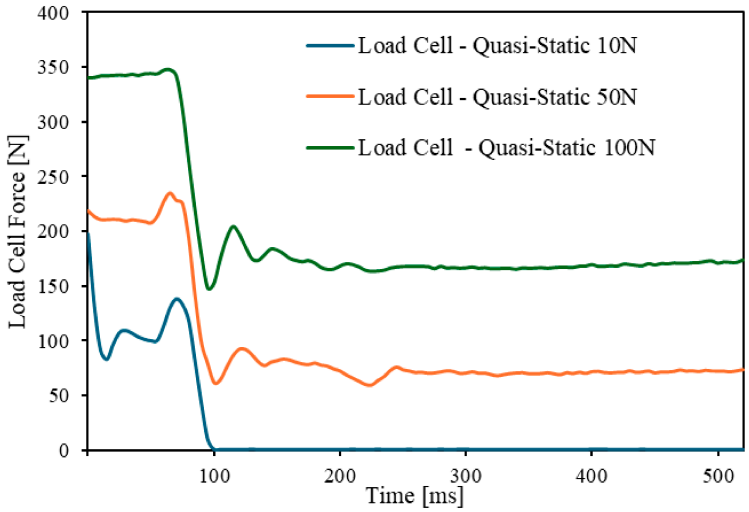


Figure 7. Force responses for quasi-static contact.

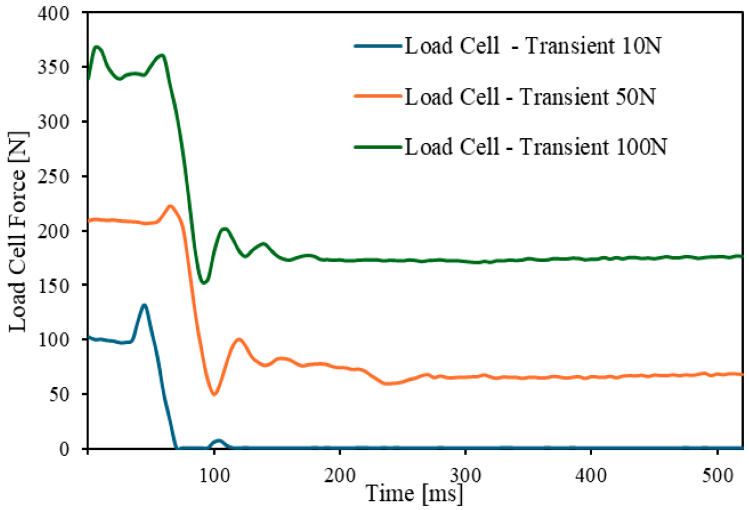


Figure 8. Force responses for transient contact.

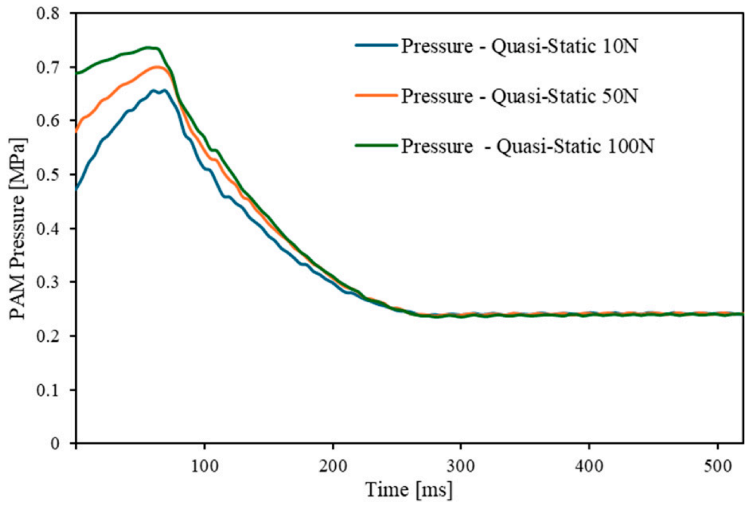


Figure 9. PAM pressure in quasi-static contact.

https://doi.org/10.3390/act15050277

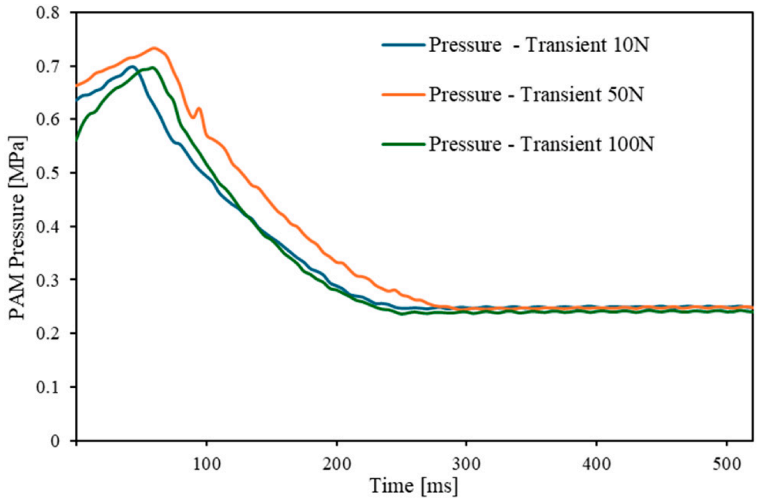


Figure 10. PAM pressure in transient contact.

3.2. Extracted Latency Metrics

Table 1 summarises the extracted timing metrics, including peak times, 90% drop times, the time to return below the pre-onset baseline force, and the FSR-derived contact release time. Across all tested scenarios, the force peak occurred within 15–20 ms after onset, while the pressure peak occurred within 5–15 ms. Force relief was rapid, 90% of the post-contact force excursion peak-to-minimum was recovered within 40–50 ms. In addition, the load-cell force returned below the baseline level within 20–35 ms after onset. Contact duration was short, the FSR signal indicated contact release within 15–45 ms in case of quasi-static impact, 15–25 ms for transient impacts. Pressure decay was significantly slower, requiring 155–180 ms for a 90% drop of the post-contact pressure excursion. Within the 5 ms timing resolution, preload primarily scaled the absolute force and pressure levels, while timing trends remained similar. Values in Table 1 were extracted from the controller-stored pointwise averaged traces of ten repeated trials per condition. Therefore, the reported values represent metrics of the averaged synchronised traces rather than trial-level statistical descriptors.

Table 1. Timing metrics extracted from measured data.

Contact Type	Preload [N]	Force Peak [N]	$\Delta t_{F,peak}$ [ms]	$\Delta t_{F,90}$ [ms]	Pressure Peak [MPa]	$\Delta t_{P,peak}$ [ms]	$\Delta t_{P,90}$ [ms]	$\Delta t_{F,base}$ [ms]	Δt_{off} [ms]
Quasi-static	10	137.8	20	45	0.656	10	170	35	45
Quasi-static	50	235.1	15	50	0.699	15	170	30	40
Quasi-static	100	347.9	15	45	0.736	5	170	20	20
Transient	10	131.4	15	40	0.697	15	170	25	25
Transient	50	223.1	15	45	0.733	10	180	25	15
Transient	100	359.8	15	45	0.696	15	155	20	15

Timing metrics extracted from the synchronised 5 ms sampled traces. All Δt values are relative to the FSR-defined contact onset instant. $\Delta t_{F,90}$ and $\Delta t_{P,90}$ refer to the time required to complete a 90% drop of the peak-to-minimum excursion after the peak. $\Delta t_{F,base}$ is the time required for the force to return below the baseline level F_{base}, mean force in the 25 ms interval preceding onset. Δt_{off} is the FSR-derived contact release time, defined by $V_{FSR}(t) < Vth$ for at least three consecutive samples.

Figure 11 compares the time to the pressure peak and the time to the force peak as functions of the preload setpoint.

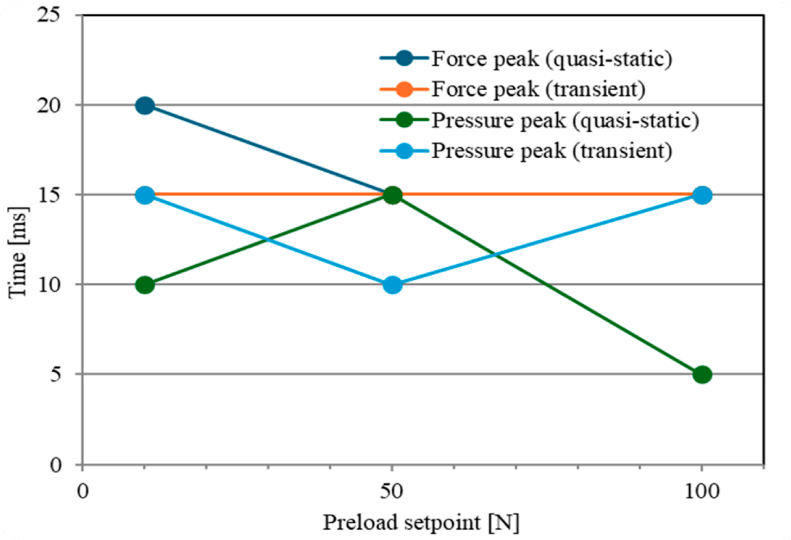


Figure 11. Time to pressure peak and force peak.

Figure 12 summarises the time required to reach a 90% drop in the force and pressure excursions.

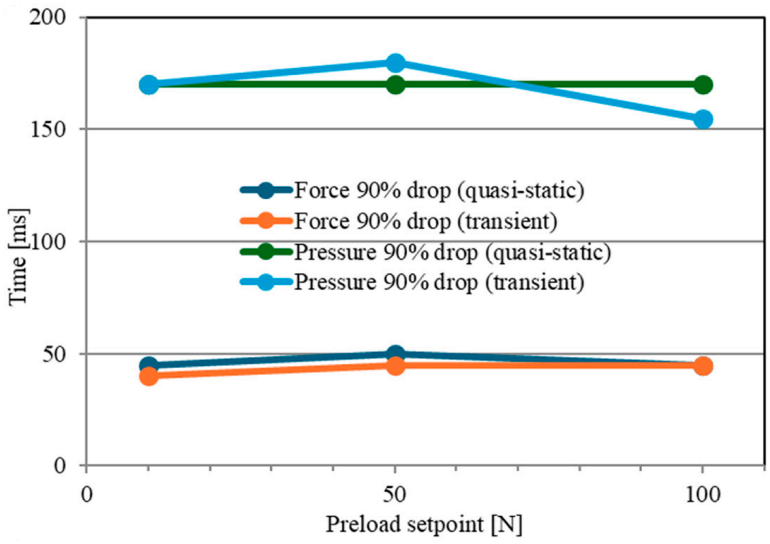


Figure 12. Time to 90% drop in force and pressure.

3.3. Severity Proxies and Sensor Correlation

In addition to timing, Table 2 reports two severity-related proxies computed from the aligned traces, the force impulse until the force peak (J_{peak}) and an early-time stiffness proxy estimated as $|\Delta F/\Delta x|$ from onset to the force peak. Reporting both absolute and baseline-referenced quantities clarifies which part of the force comes from the operating point and which part is caused by the collision. Table 2 also summarises Pearson correlation coefficients between the FSR voltage and load-cell force in a window spanning 25 ms before onset to 150 ms after onset. The correlation is moderate for quasi-static contact and lower for transient contact, indicating that the FSR provides reliable onset detection but should be combined with other modalities if force estimation is required.

Table 2. Severity proxies and sensor correlation extracted from measured data.

Contact Type	Preload [N]	F_{base} [N]	J_{peak} [N·s]	$\hat{k}$ [N/mm]	Pearson r
Quasi-static	10	105.4	2.308	5.88	0.696
Quasi-static	50	210.0	3.313	7.58	0.637
Quasi-static	100	343.2	5.188	1.91	0.510
Transient	10	98.8	1.661	9.09	0.368
Transient	50	208.4	3.196	6.32	0.433
Transient	100	342.6	5.311	4.71	0.444

F_{base} is the mean load-cell value in the 25 ms interval preceding onset. J_{peak} is the impulse computed until the force peak. $\hat{k}$, early is the early-time stiffness proxy estimated as $|\Delta F/\Delta x|$ from onset to the force peak. Pearson r denotes the correlation coefficient between the FSR voltage and the load-cell force in the evaluated time window.

Jpeak and $\hat{k}$ should be interpreted as severity-related engineering proxies. They are not injury metrics and are not directly mapped to tissue-specific biomechanical thresholds in this study. Such a mapping would require dedicated biomechanical limit selection, contact-area estimation, and body-region-specific validation.

Figure 13 illustrates the impulse accumulated until the force peak.

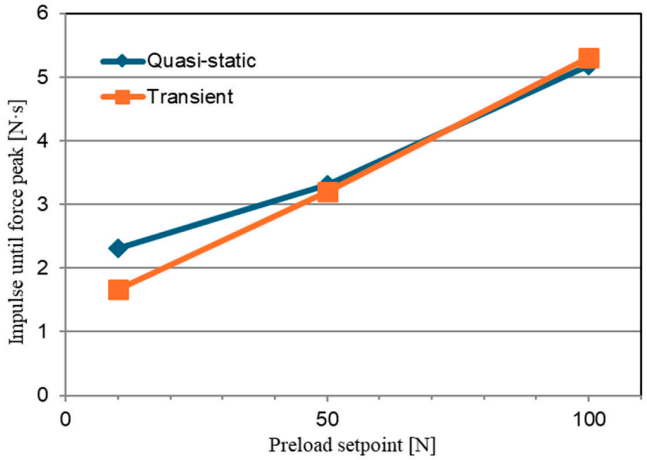


Figure 13. Impulse until the force peak.

Figure 14 reports the early-time stiffness proxy estimated from onset to the force peak.

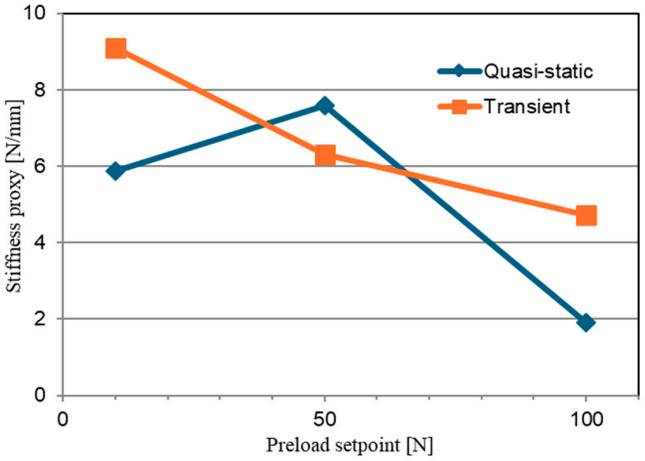


Figure 14. Early-time stiffness proxy.

4. Discussion

The measurements show that mechanical force decreases faster than pneumatic pressure. Across all tested scenarios, the load-cell force reached its first post-contact maximum within 15–20 ms after the FSR-defined onset. Because T_s = 5 ms, peak times and maxima are discretised, sub 5 ms dynamics are not resolved and peak values may be undersampled. The exact peak time may be shifted by up to one sampling interval, and the true peak amplitude may be slightly higher than the sampled value. For this reason, the results should not be used to draw conclusions about ultrafast impacts below the sampling resolution. After the peak, the force returned below the pre-onset baseline level within 20–35 ms, indicating rapid mechanical unloading relative to the operating point at onset. In contrast, the pressure peak occurred within 5–15 ms and the subsequent pressure decay required 155–180 ms to complete 90% of the post-contact excursion. The slower pressure decay is consistent with pneumatic effects such as air compressibility, finite valve flow capacity, tubing volume, and controller/valve dynamics. These contributors were not separately measured or modelled in the present work; therefore, the results identify the overall system-level pressure-decay behaviour rather than the individual delay contribution of each pneumatic component. From a safety-layer perspective, these results indicate that relying on pressure feedback alone is insufficient to certify fast mitigation; force or position sensing is needed to verify rapid unloading at the interface.

Preload increased the absolute force and pressure levels, while the extracted timing metrics remained nearly constant within the 5 ms resolution. This indicates that the measured reaction time was dominated by system-level dynamics, including controller execution, valve response, and mechanical compliance, rather than by preload-dependent actuator bandwidth. Increasing preload raised the effective stiffness and consequently the peak force level. Although the timing of unloading was similar, the impulse accumulated up to the force peak increased with preload. Since impulse is proportional to momentum change and related to energy transfer in transient contact, higher preload increases impact severity even without a change in reaction time.

The differences between quasi-static and transient contact were more pronounced in the sensor correlation than in the timing metrics. The Pearson correlation between the FSR and load cell is moderate for quasi-static contact ($r \approx 0.51$–0.70) but lower for transient contact ($r \approx 0.37$–0.44). In transient events, the contact can involve rebound, local deformation, and potential micro-slip at the interface, which can affect the FSR voltage independently of the global axial force measured by the load cell. The practical interpretation is that the FSR is effective as an onset detector but less suitable as a quantitative force estimator unless calibrated for the specific contact geometry and loading regime. Multi-modal fusion strategies that combine the FSR onset event with load-cell or model-based force estimates can therefore improve robustness.

ISO/TS 15066 emphasises that quasi-static contact can clamp tissue and thus must be evaluated separately from transient impact [1]. In the present dataset, the FSR-derived release metric indicates that contact ended within 15–45 ms after onset, 15–25 ms for transient impacts, supporting the interpretation that transient events are dominated by recoil and separation. Notably, in several cases, contact release occurred earlier than the completion of the 90% force-drop metric, which is consistent with the load cell measuring internal axial force that can remain elevated even after the external interface has separated. Within the 0.5 s observation horizon used as the transient-phase evaluation window in ISO/TS 15066, both force and pressure excursions were largely recovered. The measured timing metrics, peak within 15–20 ms, baseline recovery within 20–35 ms, and 90% force drop within 40–50 ms, are directly relevant when allocating latency budgets for protective

functions such as stop and vent routines, because they separate what must be achieved by fast detection and actuation from what is limited by pneumatic equalisation.

A limitation of the present study is that the controller retained the pointwise averaged traces rather than the individual trial records. Therefore, the present analysis focuses on representative timing and severity metrics extracted from averaged synchronised traces. Trial-level dispersion, standard deviation, confidence intervals, repeatability bands, and outlier behaviour cannot be reconstructed from the retained dataset. Future measurements should retain individual trial records to enable detailed repeatability analysis.

5. Conclusions

This paper quantified preload-dependent collision reaction timing of a PAM-actuated humanoid joint surrogate for quasi-static and transient contact. Using controller-stored averaged synchronised measurements of load-cell force, PAM pressure, position, and an FSR onset signal sampled at Ts = 5 ms, the following conclusions are drawn.

Across all tested scenarios (10 N, 50 N, and 100 N preload; quasi-static and transient contact), the load-cell force peak occurred within 15–20 ms after the FSR-defined onset.

The PAM pressure peak occurred within 5–15 ms after onset, indicating an almost immediate pressure response to contact-induced compression; however, pressure decay was slow compared to mechanical unloading.

A 90% drop of the post-contact force excursion was achieved within 40–50 ms, while the corresponding pressure excursion required 155–180 ms.

The load-cell force returned below the pre-onset baseline level within 20–35 ms. The FSR-derived contact release time was 15–45 ms (15–25 ms for transient impacts), showing that contact termination can precede full pneumatic equalisation.

Overall, the results demonstrate that the protective reaction behaviour of a PAM-actuated joint cannot be characterised from actuator properties alone; it emerges from the integrated sensing, control, pneumatic, and mechanical response of the complete system. In the tested configuration, preload primarily increased the absolute force level and the impulse accumulated before unloading, whereas the main timing trends remained comparable within the 5 ms sampling resolution. This supports the need for hardware-level validation of reaction latency in PAM-actuated humanoid joints. While the reported numerical values correspond to the investigated Festo MAS-10-40N-AA based setup, the proposed method offers a transferable experimental framework for evaluating contact onset, reaction latency, and unloading dynamics in compliant pneumatic actuation systems.

Author Contributions: Conceptualisation, D.K. and J.S.; writing—review and editing, D.K. and J.S. All authors have read and agreed to the published version of the manuscript.

Funding: This research received no external funding.

Data Availability Statement: The controller-exported pointwise averaged CSV measurement files and the processed synchronised datasets used in the present analysis are available from the corresponding author upon reasonable request. The individual trial-level time series were not retained; therefore, raw trial-by-trial dispersion data are not available.

Conflicts of Interest: The authors declare no conflicts of interest.

References

1. *ISO/TS 15066:2016*; Robots and Robotic Devices—Collaborative Robots. International Organization for Standardization: Geneva, Switzerland, 2016.
2. Bi, Z.M.; Luo, C.; Miao, Z.; Zhang, B.; Zhang, W.J.; Wang, L. Safety Assurance Mechanisms of Collaborative Robotic Systems in Manufacturing. *Robot. Comput.-Integr. Manuf.* **2021**, *67*, 102022. [CrossRef]

3. Haddadin, S.; Albu-Schäffer, A.; Hirzinger, G. Requirements for Safe Robots: Measurements, Analysis and New Insights. *Int. J. Robot. Res.* **2009**, *28*, 1507–1527. [CrossRef]
4. Lasota, P.A.; Fong, T.; Shah, J.A. A Survey of Methods for Safe Human-Robot Interaction. *Found. Trends Robot.* **2017**, *5*, 261–349. [CrossRef]
5. Haddadin, S.; Haddadin, S.; Khoury, A.; Rokahr, T.; Parusel, S.; Burgkart, R.; Bicchi, A.; Albu-Schäffer, A. On Making Robots Understand Safety: Embedding Injury Knowledge into Control. *Int. J. Robot. Res.* **2012**, *31*, 1578–1602. [CrossRef]
6. Chou, C.P.; Hannaford, B. Measurement and Modeling of McKibben Pneumatic Artificial Muscles. *IEEE Trans. Robot. Autom.* **1996**, *12*, 90–102. [CrossRef]
7. Sarosi, J.; Biro, I.; Nemeth, J.; Cveticanin, L. Dynamic Modeling of a Pneumatic Muscle Actuator with Two-Direction Motion. *Mech. Mach. Theory* **2015**, *85*, 25–34. [CrossRef]
8. Tondu, B.; Lopez, P. Modeling and Control of McKibben Artificial Muscle Robot Actuators. *IEEE Control Syst. Mag.* **2000**, *20*, 15–38. [CrossRef]
9. De Luca, A.; Mattone, R. Sensorless Robot Collision Detection and Hybrid Force/Motion Control. In Proceedings of the 2005 IEEE International Conference on Robotics and Automation, Barcelona, Spain, 18–22 April 2005; pp. 999–1004. [CrossRef]
10. De Luca, A.; Albu-Schäffer, A.; Haddadin, S.; Hirzinger, G. Collision Detection and Safe Reaction with the DLR-III Lightweight Manipulator Arm. In Proceedings of the 2006 IEEE/RSJ International Conference on Intelligent Robots and Systems, Beijing, China, 9–15 October 2006; pp. 1623–1630. [CrossRef]
11. Raiola, G.; Cardenas, C.A.; Tadele, T.S.; de Vries, T.; Stramigioli, S. Development of a Safety- and Energy-Aware Impedance Controller for Collaborative Robots. *IEEE Robot. Autom. Lett.* **2018**, *3*, 1237–1244. [CrossRef]
12. Vemula, B.; Matthias, B.; Ahmad, A. A Design Metric for Safety Assessment of Industrial Robot Design Suitable for Power- and Force-Limited Collaborative Operation. *Int. J. Intell. Robot. Appl.* **2018**, *2*, 226–234. [CrossRef]
13. Sharkawy, A.N.; Koustoumpardis, P.N. Human–Robot Interaction: A Review and Analysis on Variable Admittance Control, Safety, and Perspectives. *Machines* **2022**, *10*, 591. [CrossRef]
14. *ISO 10218-1:2025*; Robotics—Safety Requirements—Part 1: Industrial Robots. International Organization for Standardization: Geneva, Switzerland, 2025.
15. Caldwell, D.G.; Tsagarakis, N.; Medrano-Cerda, G.A. Bio-Mimetic Actuators: Polymeric Pseudo Muscular Actuators and Pneumatic Muscle Actuators for Biological Emulation. *Mechatronics* **2000**, *10*, 499–530. [CrossRef]
16. Samarathunga, S.; Valori, M.; Legnani, G.; Fassi, I. Assessing Safety in Physical Human–Robot Interaction in Industrial Settings: A Systematic Review of Contact Modelling and Impact Measuring Methods. *Robotics* **2025**, *14*, 27. [CrossRef]
17. *ISO 13482:2014*; Robots and Robotic Devices—Safety Requirements for Personal Care Robots. International Organization for Standardization: Geneva, Switzerland, 2014.
18. Giovanelli, D.; Farella, E. Force Sensing Resistor and Evaluation of Technology for Wearable Body Pressure Sensing. *J. Sens.* **2016**, *2016*, 9391850. [CrossRef]
19. Pang, G.; Yang, G.; Pang, Z. Review of Robot Skin: A Potential Enabler for Safe Collaboration, Immersive Teleoperation, and Affective Interaction of Future Collaborative Robots. *IEEE Trans. Med. Robot. Bionics* **2021**, *3*, 681–700. [CrossRef]
20. Abah, C.; Orekhov, A.L.; Johnston, G.L.H.; Simaan, N. A Multi-Modal Sensor Array for Human–Robot Interaction and Confined Spaces Exploration Using Continuum Robots. *IEEE Sens. J.* **2022**, *22*, 3585–3594. [CrossRef]
21. Klimaszewski, J.; Władziński, M. Human Body Parts Proximity Measurement Using Distributed Tactile Robotic Skin. *Sensors* **2021**, *21*, 2138. [CrossRef] [PubMed]
22. Moon, S.J.; Kim, J.; Yim, H.; Kim, Y.; Choi, H.R. Real-Time Obstacle Avoidance Using Dual-Type Proximity Sensor for Safe Human-Robot Interaction. *IEEE Robot. Autom. Lett.* **2021**, *6*, 8021–8028. [CrossRef]
23. Olugbade, T.; He, L.; Maiolino, P.; Heylen, D.; Bianchi-Berthouze, N. Touch Technology in Affective Human–, Robot–, and Virtual–Human Interactions: A Survey. *Proc. IEEE* **2023**, *111*, 1333–1354. [CrossRef]
24. Haddadin, S.; Albu-Schäffer, A.; De Luca, A.; Hirzinger, G. Collision Detection and Reaction: A Contribution to Safe Physical Human-Robot Interaction. In Proceedings of the 2008 IEEE/RSJ International Conference on Intelligent Robots and Systems, Nice, France, 22–26 September 2008; pp. 3356–3363. [CrossRef]
25. Shen, X. Nonlinear Model-Based Control of Pneumatic Artificial Muscle Servo Systems. *Control Eng. Pract.* **2010**, *18*, 311–317. [CrossRef]
26. Daerden, F.; Lefeber, D.; Verrelst, B.; Van Ham, R. Pleated Pneumatic Artificial Muscles: Actuators for Automation and Robotics. In Proceedings of the 2001 IEEE/ASME International Conference on Advanced Intelligent Mechatronics, Como, Italy, 8–12 July 2001; Volume 2, pp. 738–743. [CrossRef]
27. Palko, A.; Smrček, J. The Use of Pneumatic Artificial Muscles in Robot Construction. *Ind. Robot* **2011**, *38*, 11–19. [CrossRef]
28. Zeng, L.; Bone, G.M. Design of Elastomeric Foam-Covered Robotic Manipulators to Enhance Human Safety. *Mech. Mach. Theory* **2013**, *60*, 1–27. [CrossRef]

29. Steinecker, T.; Kurdas, A.; Mansfeld, N.; Hamad, M.; Kirschner, R.J.; Abdolshah, S.; Haddadin, S. Mean Reflected Mass: A Physically Interpretable Metric for Safety Assessment and Posture Optimization in Human-Robot Interaction. In Proceedings of the 2022 International Conference on Robotics and Automation, Philadelphia, PA, USA, 23–27 May 2022; pp. 11209–11215. [CrossRef]
30. Laudante, G.; Mirto, M.; Pennacchio, O.; Pirozzi, S. A Multi-Modal Sensing System for Human-Robot Interaction through Tactile and Proximity Data. *Front. Robot. AI* **2025**, *12*, 1581154. [CrossRef] [PubMed]
31. Kóczi, D.; Sárosi, J. Analysis of Collision Types in Collaborative Robots Using Mechanism Actuated by Pneumatic Artificial Muscle. *Actuators* **2025**, *14*, 22. [CrossRef]
32. Bíró, I.; Trojanová, M.; Čakurda, T.; Fabulya, Z.; Sárosi, J. Simulation of the Position Control of PAM, Using Its' Nonlinear Dynamic Model. *Acta Polytech. Hung.* **2023**, *20*, 103–123. [CrossRef]

Disclaimer/Publisher's Note: The statements, opinions and data contained in all publications are solely those of the individual author(s) and contributor(s) and not of MDPI and/or the editor(s). MDPI and/or the editor(s) disclaim responsibility for any injury to people or property resulting from any ideas, methods, instructions or products referred to in the content.